Effect of capillary condensation on gas transport properties in porous media

Yuta Yoshimoto,* Takuma Hori, Ikuya Kinefuchi,† and Shu Takagi
Department of Mechanical Engineering, The University of Tokyo, 7-3-1 Hongo, Bunkyo-ku, Tokyo 113-8656, Japan
(Received 29 June 2017; revised manuscript received 2 October 2017; published 30 October 2017)

We investigate the effect of capillary condensation on gas diffusivity in porous media composed of randomly packed spheres with moderate wettability. To simulate capillary phenomena at the pore scale while retaining complex pore networks of the porous media, we employ density functional theory (DFT) for coarse-grained lattice gas models. The lattice DFT simulations reveal that capillary condensations preferentially occur at confined pores surrounded by solid walls, leading to the occlusion of narrow pores. Consequently, the characteristic lengths of the partially wet structures are larger than those of the corresponding dry structures with the same porosities. Subsequent gas diffusion simulations exploiting the mean-square displacement method indicate that while the effective diffusion coefficients significantly decrease in the presence of partially condensed liquids, they are larger than those in the dry structures with the same porosities. Moreover, we find that the ratio of the porosity to the tortuosity factor, which is a crucial parameter that determines an effective diffusion coefficient, can be reasonably related to the porosity even for the partially wet porous media.

DOI: 10.1103/PhysRevE.96.043112

I. INTRODUCTION

Gas diffusion in porous media is an important phenomenon for the design of adsorbents [1,2], permeation membranes [3,4], and fuel cell electrodes [5–7] with the complex void labyrinths of porous media significantly hindering internal gas diffusion. Typically, effective diffusion coefficients inside porous media can be measured using countercurrent gas diffusion in the Wicke-Kallenbach or Graham's diffusion cell [8,9]. Nevertheless, detailed information about the pore space is required to relate the microscopic features of the porous media to the effective diffusivity, which serves as the guiding parameter for the design of porous media. To obtain such information, imaging techniques such as x-ray computer tomography [5,10–12] and scanning electron microscopy combined with focused ion beam milling [7,13–15] have been widely utilized to reconstruct porous media based on real structures. Although these experimental methods can successfully elucidate the microscopic features of realistic porous media, they intrinsically require time-consuming processes such as preparation and destruction of the observation objects, followed by image processing prior to the reconstruction. *In silico* structural reconstruction of a porous medium combined with subsequent gas diffusion simulation is a promising alternative choice to perform extensive studies of the relationship between the microscopic features of the pore network and the effective diffusivity. Indeed, a number of researchers have studied gas diffusions in the numerically constructed porous media composed of randomly packed spheres [6,16–18] or random fiber structures [19,20]. One of the important findings for the porous media composed of randomly packed spheres is that the tortuosity factor, which represents the tortuous nature of a pore network and determines effective diffusivity, can be well defined as a purely structural parameter as long as the porosity is higher than 0.1 and the characteristic length is appropriately chosen [17,18].

From a practical point of view, gas diffusion in the presence of partially condensed liquids is a common phenomenon in porous media. For example, a catalyst layer of a polymer electrolyte fuel cell during high-power operation inevitably suffers from water-flooding issues due to capillary condensation of water vapor that results in a significant increase in the oxygen diffusion resistance [21,22]. Experimentally, radiography techniques employing neutrons [23], synchrotron x rays [24], and soft x rays [25] have been utilized for *in situ* visualization of water distribution in a porous medium. However, the finest available resolution, achieved using the soft x-ray radiography technique, is at the submicron scale, which is insufficient for characterizing capillary phenomena in microporous and mesoporous materials. Meanwhile, a number of simulation studies have been dedicated to capillary phenomena in porous media [26–28]; however, little attention has been paid to the effects of these phenomena on gas diffusivity [29,30]. Therefore, the present study aims to numerically elucidate the effect of capillary condensation on gas transport properties in porous media. We should note that the classical density functional theory (DFT) [31–37] and molecular simulation techniques [38–40] are useful for understanding the thermodynamics and phase behavior of confined fluids, but cannot be applied to large-scale porous media with complex pore networks due to their high computational costs. Alternatively, we employ the lattice DFT [28,41–44] to simulate capillary condensation inside porous media composed of randomly packed spheres. The lattice DFT is a coarse-grained version of the conventional DFT, thus allowing for the simulation of capillary phenomena at the pore scale while retaining the complex pore networks of the porous media. Subsequently, gas diffusion in the presence of partially condensed liquids is evaluated using the mean-square displacement method [45,46]. Finally, we discuss the ratio of the porosity ε to the tortuosity factor τ, which is a crucial parameter that determines effective diffusivity in porous media.

The remainder of this paper is organized as follows. In Sec. II, we describe in detail the methods for the construction of model porous media, thereby simulating capillary condensation using the lattice DFT. We then describe the procedure for

*yyoshimoto@fel.t.u-tokyo.ac.jp
†kine@fel.t.u-tokyo.ac.jp

obtaining effective diffusion coefficients and tortuosity factors of the porous media. Section III presents the obtained results and the discussion, where a special emphasis is placed on the differences between the dry and partially wet structures to highlight the effect of capillary condensation. Concluding remarks are presented in Sec. IV.

II. METHODS

A. Numerical construction of porous media

Model porous media are constructed using the drop-and-roll algorithm [6,16–18]. The domain size is $160L\times160L\times600L$ with periodic boundary conditions in horizontal (xy) directions, where L corresponds to a side length of the cubic lattice in the lattice DFT simulation described in Sec. II B. The sphere diameter is $10L$. At each trial, the initial horizontal position located at $0 < x < 160L$ and $0 < y < 160L$ is randomly assigned to a single sphere using the uniform random numbers. Then the sphere is dropped far from the top of the domain in the z direction. When the incoming sphere contacts an already packed sphere(s), it rotates around the contacting sphere(s). This process is repeated until the incoming sphere hits the floor ($z = 0$) or is placed at a stable position, where it is supported by three other spheres and the projection of its center on the horizontal plane is located within the triangle formed by the projections of three contacting points. The next trial starts after the incoming sphere settles into a stable position. This drop-and-roll process is repeated until the z coordinate of the center of the topmost sphere exceeds the top of the domain ($z = 600L$). Then the bottom ($0 < z < 60L$) and the top ($540L < z < 600L$) regions are removed from the domain to eliminate the effects of the floor and top layer. Finally, we obtain the model porous medium with the domain size of $160L\times160L\times480L$, as displayed in Fig. 1.

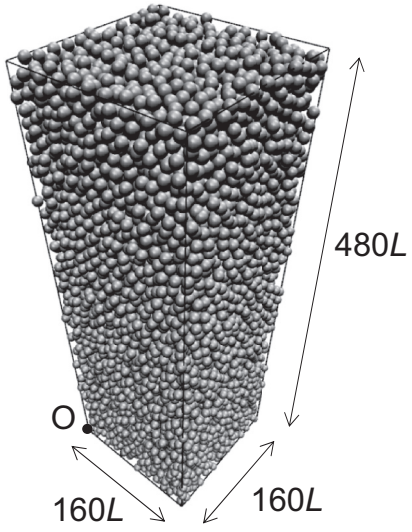

FIG. 1. Representative porous medium constructed using the drop-and-roll algorithm with the sphere diameter $10L$. Domain dimensions are $160L\times160L\times480L$ with the periodic boundary conditions in the horizontal directions. The origin of the coordinates is located at a vertex of the bottom plane. The contact angle and porosity are 0° and 0.42.

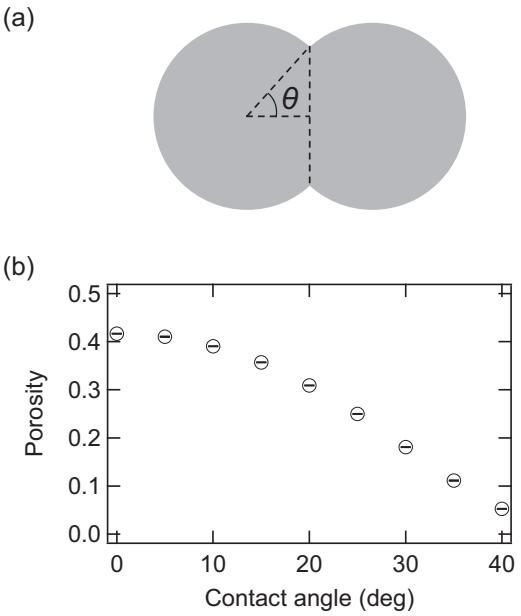

FIG. 2. (a) Definition of contact angle θ between two contacting spheres. The contact angle is spanned by the two lines, one of which connects the sphere center with the center of the contact area, and the other with the circumference of the contact area. (b) Porosity as a function of the contact angle. The error bars of each marker are standard deviations obtained using five different structures.

The porosity of the porous medium can be tuned using the contact angle between two contacting spheres [6], as displayed in Fig. 2(a). The contact angle is kept constant throughout the construction process. The porosity is obtained by randomly dropping $200N_s$ test points inside the domain, where N_s is the number of spheres, and then calculating the fraction of the test points in a void space. The porosity is shown as a function of the contact angle in Fig. 2(b). The porosity decreases with the increasing contact angle, indicating good agreement with the results obtained in a previous study [6]. The error bars of each marker are obtained from five different structures and exhibit negligibly small fluctuations. In the present study, we focus on the porous media with porosities higher than 0.1, where the tortuosity factor shows little dependence on the Knudsen number $\mathrm{Kn} \equiv \xi/d$ [17,18]. Here ξ is the mean free path of the gas molecules and d is the characteristic length of the porous medium.

Finally, the model porous media are discretized into cubic lattices with the side length L to be utilized in the subsequent lattice DFT simulations of capillary condensation. It should be noted that the porosities of discretized structures are almost identical to those of the original structures, exhibiting deviations of at most 0.1% only. Hereafter, the length scale is expressed in units of L (i.e., $L = 1$).

B. Simulation of capillary condensation based on the lattice density functional theory

Lattice DFT is based on the mean-field lattice gas model [28,41–44] and can be viewed as a coarse-grained version of the conventional DFT [31–37]. In the lattice DFT scheme, the system of interest is discretized into lattices that correspond

to either a solid or a fluid site, where both the fluid-fluid and solid-fluid interactions are treated for the nearest neighbor sites, thus enabling a far larger simulation scale than that of the conventional DFT. The density distribution $\{\rho\}$ is obtained by minimizing the grand potential of the system with respect to the density $\rho_{\mathbf{i}}$, where $\mathbf{i}$ denotes the position vector of each fluid site and $\rho_{\mathbf{i}}$ varies from 0 to 1. The grand potential $\Omega(\{\rho\})$ is given by

$$\Omega(\{\rho\}) = k_{\mathrm{B}}T \sum_{\mathbf{i}} [\rho_{\mathbf{i}} \ln \rho_{\mathbf{i}} + (1-\rho_{\mathbf{i}}) \ln (1-\rho_{\mathbf{i}})] - \frac{\varepsilon_{\mathrm{ff}}}{2} \sum_{\mathbf{i}} \sum_{\mathbf{a}} \rho_{\mathbf{i}} \rho_{\mathbf{i}+\mathbf{a}} + \sum_{\mathbf{i}} \rho_{\mathbf{i}} (\varphi_{\mathbf{i}} - \mu), \quad (1)$$

where k_{B} is the Boltzmann constant, T is the thermodynamic temperature, $\varepsilon_{\mathrm{ff}}$ is the fluid-fluid interaction parameter, $\mathbf{a}$ is the vector from site $\mathbf{i}$ to the nearest neighbor, and μ is the chemical potential. $\varphi_{\mathbf{i}}$ is the external field exerted on the fluid site $\mathbf{i}$ from the nearest solid site and is given by

$$\varphi_{\mathbf{i}} = -\sum_{\mathbf{a}} \chi(\mathbf{i},\mathbf{a}) \varepsilon_{\mathrm{sf}}, \quad (2)$$

where $\varepsilon_{\mathrm{sf}}$ is the solid-fluid interaction parameter, and $\chi = 1$ if $(\mathbf{i}+\mathbf{a})$ is a solid site and $\chi = 0$ otherwise. Then the equilibrium density distribution is obtained by

$$\left(\frac{\partial \Omega}{\partial \rho_{\mathbf{i}}}\right)_{\mu,\{\varphi\},T} = 0 \quad \text{for} \quad \forall\, \mathbf{i}. \quad (3)$$

Substitution of Eq. (1) into Eq. (3) yields

$$k_{\mathrm{B}}T \ln\left(\frac{\rho_{\mathbf{i}}}{1-\rho_{\mathbf{i}}}\right) - \varepsilon_{\mathrm{ff}} \sum_{\mathbf{a}} \rho_{\mathbf{i}+\mathbf{a}} + \varphi_{\mathbf{i}} - \mu = 0 \quad \text{for} \quad \forall\, \mathbf{i}. \quad (4)$$

This equation can be further reformulated into

$$\rho_{\mathbf{i}} = \frac{\lambda c_{\mathbf{i}}}{1+\lambda c_{\mathbf{i}}} \quad \text{for} \quad \forall\, \mathbf{i}, \quad (5)$$

where

$$\lambda \equiv \exp\left(\frac{\mu}{k_{\mathrm{B}}T}\right), \quad (6)$$

$$c_{\mathbf{i}} \equiv \exp\left[-\frac{1}{k_{\mathrm{B}}T}\left(\varphi_{\mathbf{i}} - \sum_{\mathbf{a}} \rho_{\mathbf{i}+\mathbf{a}}\right)\right]. \quad (7)$$

Here, the activity λ is uniform throughout the system at equilibrium. Therefore, once the chemical potential is specified, the equilibrium density distribution can be obtained by iteratively solving Eqs. (5) and (7) until converged solutions are attained. Practically, by gradually changing λ, the density distribution for the previous λ can be utilized as an initial guess for the current λ, allowing for fast convergence. Hereafter, we introduce the relative activity λ/λ_0, where λ_0 is the activity at bulk saturation given by $\lambda_0 = \exp(-3\varepsilon_{\mathrm{ff}}/k_{\mathrm{B}}T)$ in the lattice gas model [28,47]. We note that the relative activity is essentially equivalent to the relative pressure apart from the effect of gas imperfection.

The phase behavior of the lattice DFT system is characterized by the reduced temperature $T^* \equiv k_{\mathrm{B}}T/\varepsilon_{\mathrm{ff}}$ and the wettability parameter $\alpha \equiv \varepsilon_{\mathrm{sf}}/\varepsilon_{\mathrm{ff}}$. In the present study, we set $T^* = 1$ and $\alpha = 1$, corresponding to moderate wettability between the fluid and solid phases. The simulation system is shown in Fig. 3. The porous medium with the contact angle of 0° is immersed in the system with the dimensions of $320L \times 320L \times 960L$, ensuring a sufficiently large bulk fluid region. Here, L is the side length of each cubic lattice. The adsorption process is simulated by gradually increasing the relative activity from 0 to 1.0 and vice versa for the desorption process.

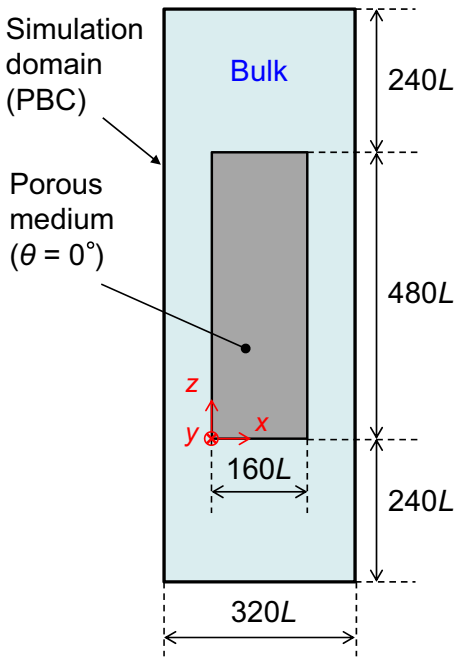

FIG. 3. Lattice DFT simulation system. The porous medium with the contact angle 0° is immersed in the system with the volume of $320L \times 320L \times 960L$, where the side length of each cubic lattice is L. Periodic boundary conditions (PBCs) are imposed in all directions.

C. Calculation of effective diffusion coefficients and porosity-to-tortuosity ratios

The effective diffusion coefficient D_{e} in a porous medium has been often represented by [17,18]

$$D_{\mathrm{e}}(\mathrm{Kn}) = \frac{\varepsilon}{\tau} D_0(\mathrm{Kn}), \quad (8)$$

where ε is the porosity and τ is the tortuosity factor. D_0 is the diffusion coefficient obtained for a nonporous structure and is given by [48]

$$D_0(\mathrm{Kn}) = \left(\frac{1}{D_{\mathrm{b}}} + \frac{1}{D_{\mathrm{K}}}\right)^{-1} = \frac{D_{\mathrm{b}}}{1+\mathrm{Kn}} = \frac{D_{\mathrm{K}}}{1+\mathrm{Kn}^{-1}}. \quad (9)$$

The bulk diffusion coefficient D_{b} is $\xi v/3$ and the Knudsen diffusion coefficient D_{K} is $dv/3$, where v denotes the mean thermal velocity of the gas molecules. Note that $D_0(\mathrm{Kn} \to 0) = D_{\mathrm{b}}$ and $D_0(\mathrm{Kn} \to \infty) = D_{\mathrm{K}}$.

In principle, the tortuosity factor τ is a structural parameter that characterizes the nature of the void network such as twists and turns, and should not be dependent on the flow regime. For the porous media composed of randomly packed

spheres with porosities >0.1, it has been reported that the tortuosity factors can be well defined as purely structural parameters independent of the Knudsen number Kn as long as the characteristic length d is appropriately chosen according to [17,18]

$$d = \left(\frac{\langle l^2 \rangle}{2\langle l \rangle^2} - \beta \right) \langle l \rangle, \tag{10}$$

where $\langle l \rangle$ is the mean of the chord length distribution, $\langle l^2 \rangle$ is the mean of the second moment of the distribution, and β represents the redirection effect of free molecules colliding only with the pore wall [49–52]. More specifically, β is given by

$$\beta = -\sum_{m=1}^{\infty} \langle \cos \gamma_m \rangle, \tag{11}$$

where $\langle \cos \gamma_m \rangle$ is the mean value of the cosine of the angle γ_m between the two trajectories separated by m wall collisions.

Equation (8) indicates that the ratio of the porosity to the tortuosity factor, ε/τ, is a crucial parameter that determines the effective diffusion coefficient in a porous medium. To evaluate the ratio ε/τ from Eq. (8), we calculate the effective diffusion coefficients in the Knudsen flow regime, $D_e(\mathrm{Kn} \to \infty)$, using the mean-square displacement (MSD) method [45,46]. The effective diffusion coefficient D_e can be obtained by

$$D_e = \varepsilon \lim_{t \to \infty} \frac{\langle |\mathbf{r}(t) - \mathbf{r}(0)|^2 \rangle}{6t}, \tag{12}$$

where $\mathbf{r}(t)$ is the position of a gas molecule at time t. To calculate the MSD, 10 000 test molecules are randomly inserted into the void space of the porous medium with a volume of $160L \times 160L \times 480L$ and subsequently allowed to fly inside the pore network and reflect at the pore walls following the Knudsen cosine law [53,54]. Periodic boundary conditions are imposed in the x and y directions, whereas a mirror boundary condition is imposed in the z direction. Since the mirror boundary condition may slightly affect the MSD [6], the molecules are initially dropped into a central portion of the structure ($160L < z < 320L$) to alleviate the effects of the top and bottom boundaries. Unless otherwise stated, the molecules are allowed to fly for a cumulative distance 625 times as large as the side length of the simulation domain in the horizontal direction, $160L$, ensuring that sufficiently large regions are explored by the test molecules. Hereafter, the time unit is chosen as L/v.

III. RESULTS AND DISCUSSION

A. Capillary condensation in the porous medium

Figure 4 shows the adsorption and desorption isotherms for the porous medium with $\theta = 0^\circ$ obtained from the lattice DFT simulations. In the adsorption process, the mean density of fluid sites increases with the relative activity λ/λ_0, exhibiting an especially sharp increase around $\lambda/\lambda_0 = 0.6$–0.8. In the desorption process, the mean density decreases slightly prior to the abrupt decrease at $\lambda/\lambda_0 \sim 0.66$, showing a different path from the adsorption isotherm. This hysteresis loop is very similar to the H2(a)-type hysteresis, typical of many silica gels, some porous glasses, and some ordered mesoporous materials with pore diameters in the range of 2–50 nm [55]. The very steep desorption branch can be attributed either to pore blocking or percolation in narrow pore necks or to cavitation-induced evaporation. The right axis of Fig. 4 displays the apparent porosity during the adsorption process calculated on the assumption that the fluid sites with densities >0.5 are occluded by the condensed liquids. The apparent porosity decreases sharply around $\lambda/\lambda_0 = 0.6$–0.8 in accordance with the increase in the mean fluid density and becomes almost 0 at $\lambda/\lambda_0 = 1.0$. Strictly speaking, the appropriate threshold of fluid density for defining the gas and liquid phases is not well defined in confined systems. However, it should be noted that in the lattice gas model, a bulk fluid is a liquid if the density is more than 0.5 and is a gas otherwise [56].

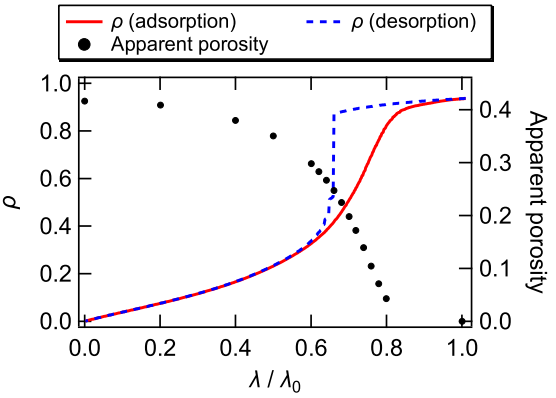

FIG. 4. Adsorption and desorption isotherms for the porous medium with $\theta = 0^\circ$. Left axis shows the mean density of fluid sites in the structure. Right axis shows the apparent porosity during the adsorption process calculated on the assumption that the fluid sites with the densities >0.5 are occluded by condensed liquids.

Fluid density distributions during the adsorption process are indicated in Fig. 5. As the relative activity increases, capillary condensations preferentially occur at confined pores surrounded by the solid walls, leading to the occlusion of narrow pores. A further increase in the relative activity induces the formation of liquid bridges between condensed liquids, giving rise to the liquid network.

B. Structural characterizations of partially wet structures

In the partially wet porous media through the adsorption process, the fluid sites with densities >0.5 are regarded as condensed liquids that inhibit gas diffusion and are hereafter treated in the same manner as the solid sites. Chord length distributions of the dry and partially wet structures are calculated by randomly drawing 6 000 000 lines and extracting the segments located in void spaces [57], as shown in Fig. 6. Both chord length distributions exhibit spikes at the chord length l equal to integer values due to the lattice discretization of the structures. The frequency around $1 < l < 3.5$ for $\lambda/\lambda_0 = 0.74$ is smaller than that for $\lambda/\lambda_0 = 0$, indicating the occlusions of narrow pores due to capillary condensations.

To further highlight the effect of capillary condensation on the structural properties, we compare chord length distributions between the partially wet structures and dry structures

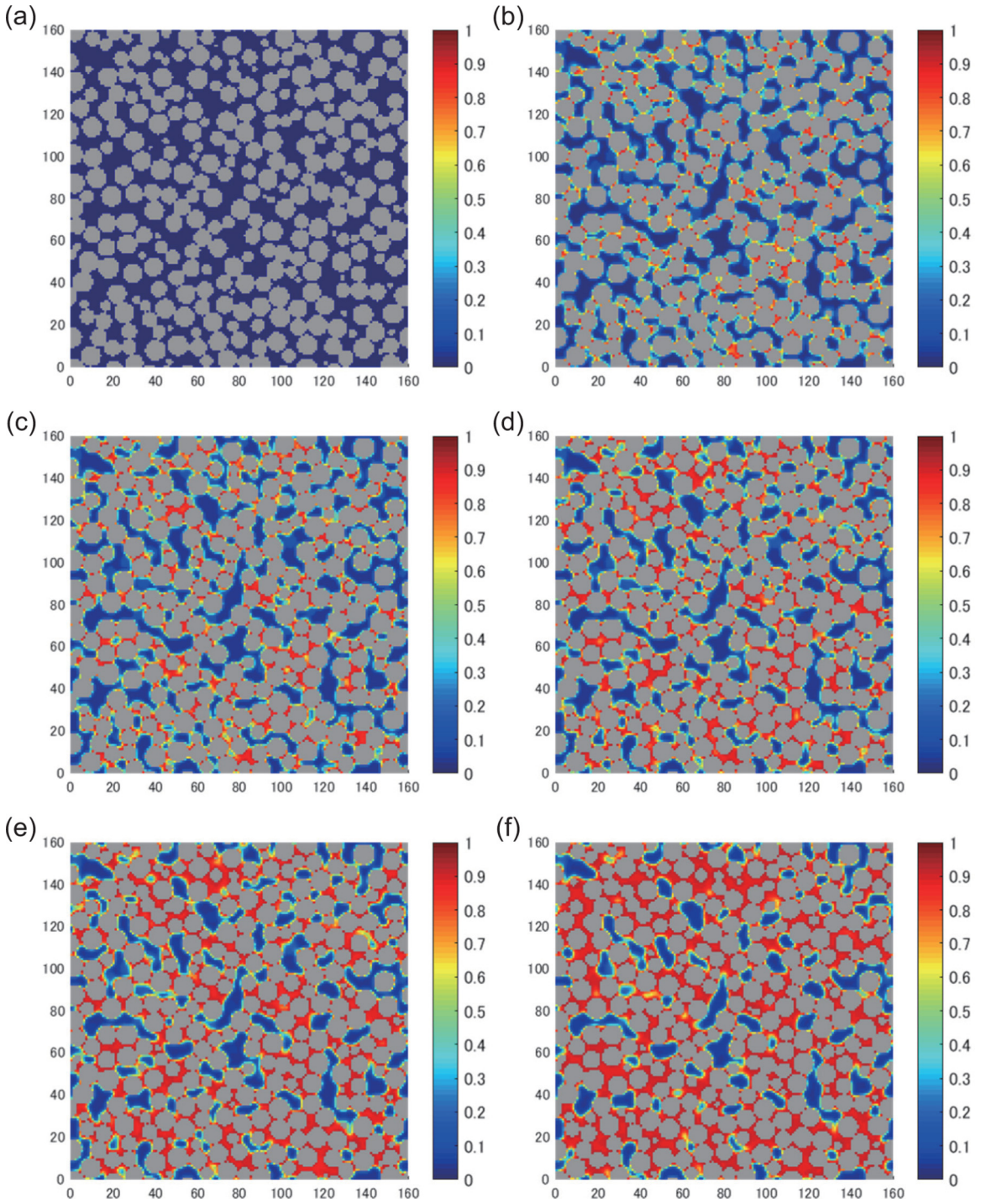

FIG. 5. Fluid density distributions in the plane of $z = 240L$ during the adsorption process. Gray regions correspond to solids. (a) Relative activity $\lambda/\lambda_0 = 0$ and apparent porosity $\varepsilon_a = 0.42$, (b) $\lambda/\lambda_0 = 0.50$ and $\varepsilon_a = 0.35$, (c) $\lambda/\lambda_0 = 0.60$ and $\varepsilon_a = 0.30$, (d) $\lambda/\lambda_0 = 0.66$ and $\varepsilon_a = 0.25$, (e) $\lambda/\lambda_0 = 0.70$ and $\varepsilon_a = 0.20$, and (f) $\lambda/\lambda_0 = 0.74$ and $\varepsilon_a = 0.14$.

with the same porosities. The partially wet structures for $\lambda/\lambda_0 = 0.50$, 0.60, 0.66, 0.70, and 0.74 correspond to the dry structures with $\theta = 15.8°$, 21°, 25.2°, 28.8°, and 33°, where the porosities are 0.35, 0.30, 0.25, 0.20, and 0.14, respectively. Figure 7 shows examples of the chord length distributions of the dry and partially wet structures with the same porosities. Clearly, small pores in the partially wet structures are occluded by capillary condensations, resulting in the lower frequencies of the narrow pores ($l < 3$) and the higher frequencies of the large pores ($l > 3$) compared to the dry structures.

Figure 8 summarizes the structural parameters of the dry and partially wet structures. The mean chord length of the dry structure with $\varepsilon = 0.42$ is about $3.5L$ as shown in Fig. 8(a). Interestingly, the mean chord lengths of the partially wet structures show little dependence on λ/λ_0, exhibiting a slight increase from $\lambda/\lambda_0 = 0(\varepsilon = 0.42)$ to $\lambda/\lambda_0 = 0.50(\varepsilon = 0.35)$

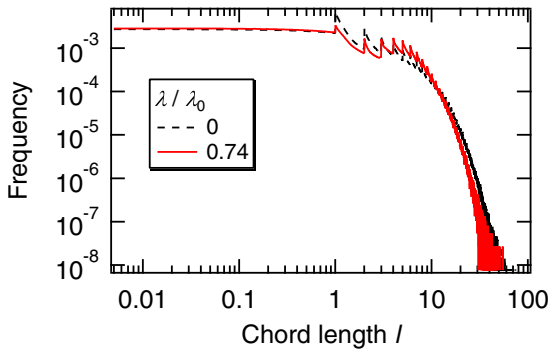

FIG. 6. Chord length distributions of the dry ($\lambda/\lambda_0 = 0$) and partially wet ($\lambda/\lambda_0 = 0.74$) structures with $\theta = 0^\circ$.

and almost the same values for $\lambda/\lambda_0 > 0.50$, even though the porosity decreases with increasing λ/λ_0. This is in contrast to the cases for the dry structures, where a decrease in the porosity accompanied by increasing θ significantly affects the mean chord length. The main reason for this difference is that occlusions of narrow pores in the partially wet structures lead to the low frequencies of the narrow pores and thus the relatively higher frequencies of the large pores, as discussed above. Figure 8(b) shows the ratio $\langle l^2\rangle/2\langle l\rangle^2$ which appears in Eq. (10). Although $\langle l^2\rangle/2\langle l\rangle^2$ shows a slight dependence on the porosity for the dry structures, it is almost unity for all dry structures, implying that their chord length distributions

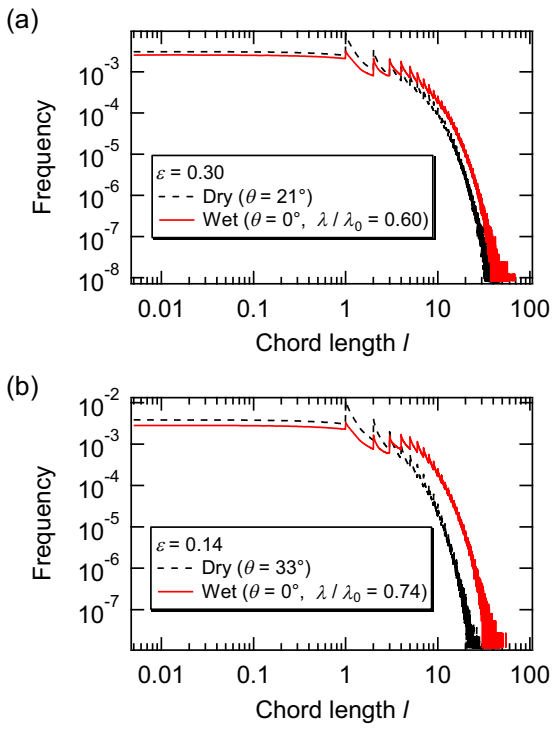

FIG. 7. Comparison of chord length distributions between the dry and partially wet structures with the same porosities. (a) Dry structure with $\theta = 21^\circ$ and partially wet structure with $\theta = 0^\circ$ and $\lambda/\lambda_0 = 0.60$, both of which have $\varepsilon = 0.30$; (b) dry structure with $\theta = 33^\circ$ and the partially wet structure with $\theta = 0^\circ$ and $\lambda/\lambda_0 = 0.74$, both of which have $\varepsilon = 0.14$.

are close to an exponential distribution [17,58]. By contrast, $\langle l^2\rangle/2\langle l\rangle^2$ of the partially wet structures differs from unity more remarkably, indicating that the chord length distributions of the partially wet structures show greater deviations from the exponential distribution as λ/λ_0 increases. In addition, following Ref. [17], the parameters β of all structures are calculated using the first 12 terms of Eq. (11), where $\langle\cos\gamma_m\rangle$ is obtained from the Knudsen diffusion simulations presented in Sec. III C. Figure 8(c) indicates that β values of the partially wet and dry structures are almost identical and are larger than the theoretical value of 4/13 for the Knudsen cosine law in random packings of monodisperse spheres [17]. The latter tendency is typical of lattice discretized structures and has also been reported in a previous study [18].

Eventually, we can obtain the characteristic lengths d for the corresponding structures via Eq. (10) with the above structural parameters, as shown in Fig. 8(d). Notably, while the d values of the dry structures decrease sharply with decreasing porosity, those of the partially wet structures show a more moderate dependence on the apparent porosity. This is mainly due to the differences of the mean chord lengths between the dry and partially wet structures, as shown in Fig. 8(a). As a consequence, the d values of the partially wet structures are significantly larger than those of the dry structures, especially for the lower porosities.

C. Effective diffusion coefficients and porosity-to-tortuosity ratios

The MSDs in the dry ($\lambda/\lambda_0 = 0$) and partially wet ($\lambda/\lambda_0 = 0.60$, 0.70, and 0.74) structures with $\theta = 0^\circ$ are indicated in Fig. 9. Since an increase in λ/λ_0 hinders the gas diffusion significantly, it takes a longer time for the gas molecules to reach normal diffusions, where the MSDs are proportional to time t. Especially for $\lambda/\lambda_0 = 0.74$ corresponding to $\varepsilon = 0.14$, it is necessary to run the simulations for as long as $t = 10^6$ to obtain the normal diffusion [see Fig. 10(b)]. Accordingly, we extract the normal diffusion regimes from $t = 8\times10^4$ to 1×10^5 for $\varepsilon = 0.20$–0.42, and from $t = 8\times10^5$ to 1×10^6 for $\varepsilon = 0.14$ to obtain diffusion coefficients.

To further investigate the effect of capillary condensation on gas diffusivity, we compare MSDs of the partially wet structures and those of dry structures with the same porosities, as shown in Fig. 10. Even for the same porosities, the gas diffusivities in the partially wet structures are larger than those in the dry structures. This tendency becomes more pronounced as the porosity decreases as shown in Fig. 11(a) where the effective diffusion coefficients in the dry and partially wet structures with the same porosities are presented. Finally, Fig. 11(b) compares the ratio of the porosity to the tortuosity factor, ε/τ, of the dry and partially wet structures with the same porosities based on Eq. (8). Notably, the ε/τ values show little dependence on whether the structure is dry or partially wet, and can be reasonably related to the porosity, although a slight difference between the dry and partially wet structures is observed at $\varepsilon = 0.14$. This is because while the effective diffusion coefficients in the partially wet structures are larger than those in the dry structures as shown in Fig. 11(a), the diffusion coefficients $D_0(\mathrm{Kn}\to\infty) = D_K = dv/3$ defined by Eq. (9) are also larger for the partially wet structures as shown

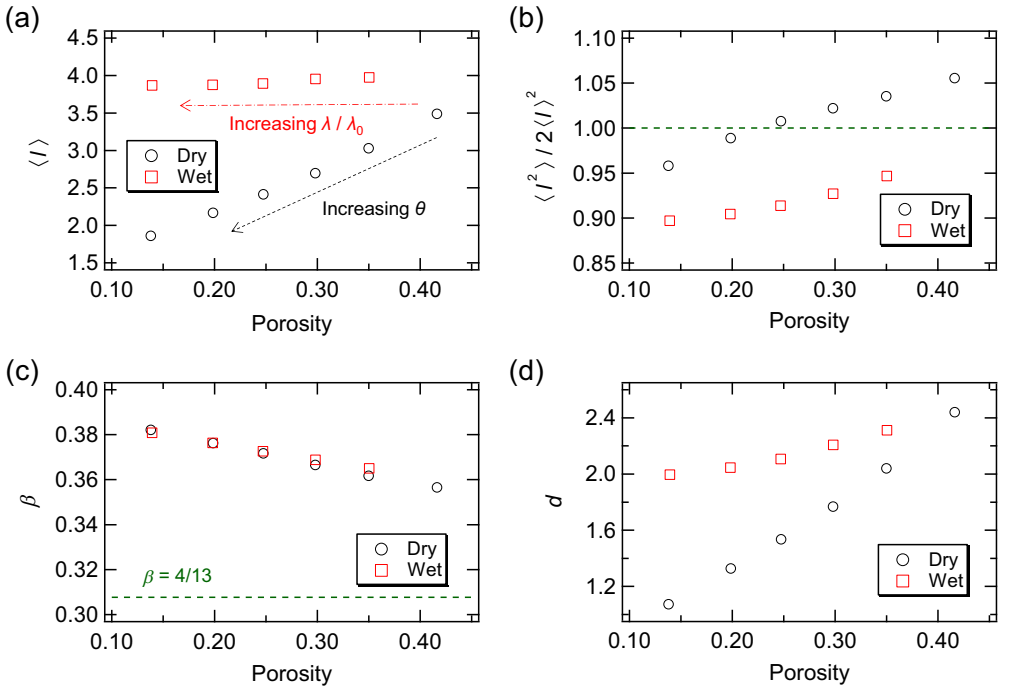

FIG. 8. Structural parameters of the dry and partially wet structures. Contact angle θ is varied for the dry structures, while θ is kept at 0° and λ/λ_0 is varied for all partially wet structures. (a) Mean chord length $\langle l \rangle$, (b) the ratio $\langle l^2 \rangle / 2\langle l \rangle^2$ in Eq. (10) with the theoretical value 1 for an exponential chord length distribution indicated by a dashed line, (c) β given by Eq. (11) with the theoretical value 4/13 for the Knudsen cosine law in random packings of monodisperse spheres indicated by a dashed line, and (d) characteristic length d given by Eq. (10).

in Fig. 8(d), thus resulting in almost identical values of ε/τ for the dry and partially wet structures.

From the practical point of view, the present study implies the possibility of estimating the value of ε/τ of a partially wet porous medium with certain apparent porosity measured experimentally using volumetric or gravimetric methods [59,60], according to the available value of ε/τ of a dry porous medium with the same material and porosity. However, for a definitive conclusion, further studies exploiting other types of porous media [19,20] are required in future. In addition, since all porous media in the present study are discretized into cubic lattices for the lattice DFT simulations, the values of ε/τ differ from those of nonlattice structures. Nevertheless, the fact that the values of ε/τ are almost the same between dry and partially wet structures may also hold for the nonlattice structures.

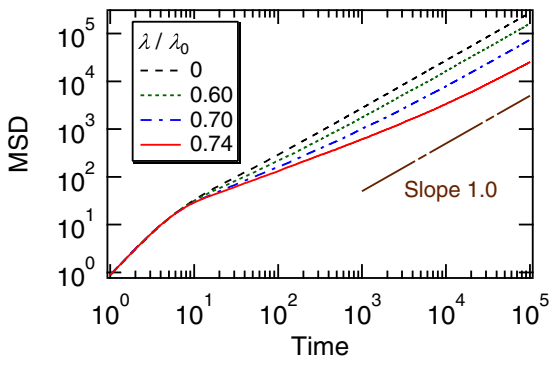

FIG. 9. MSDs (on a log-log scale) in the dry ($\lambda/\lambda_0 = 0$) and partially wet ($\lambda/\lambda_0 = 0.60$, 0.70, and 0.74) structures with $\theta = 0°$.

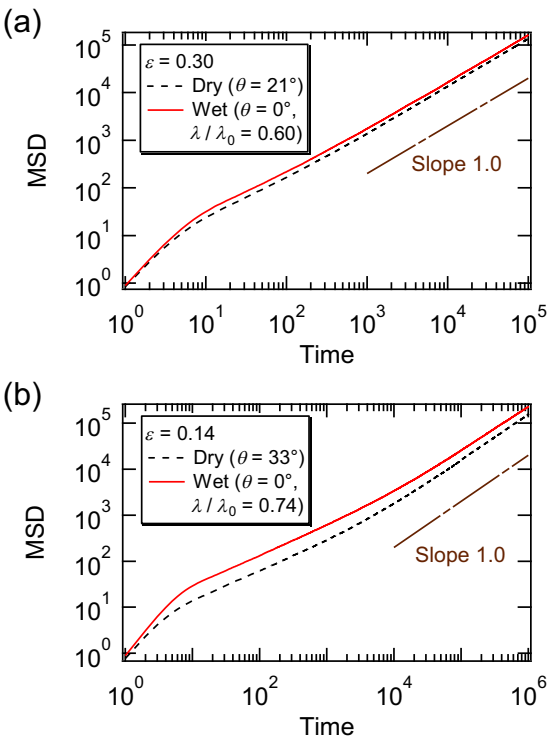

FIG. 10. Comparison of the MSDs (on a log-log scale) between the dry and partially wet structures with the same porosities. (a) Dry structure with $\theta = 21°$ and the partially wet structure with $\theta = 0°$ and $\lambda/\lambda_0 = 0.60$, both of which have $\varepsilon = 0.30$; (b) dry structure with $\theta = 33°$ and the partially wet structure with $\theta = 0°$ and $\lambda/\lambda_0 = 0.74$, both of which have $\varepsilon = 0.14$.

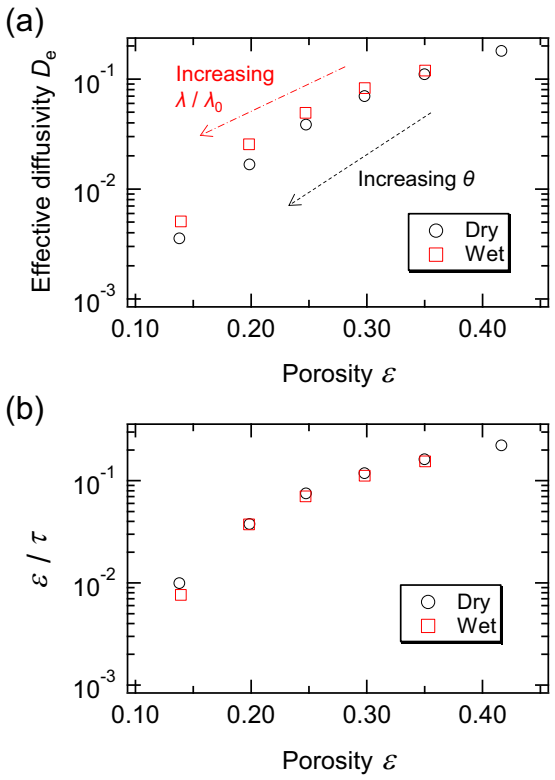

FIG. 11. Effective diffusion coefficients obtained from the slopes of the MSDs based on Eq. (12) (a) and the ratio of a porosity ε to the tortuosity factor τ (b) of the dry and partially wet structures with the same porosities. Contact angle θ is varied for the dry structures, while θ is kept at 0° and λ/λ_0 is varied for all the partially wet structures.

It should also be noted that to estimate an effective diffusion coefficient D_e(Kn) for certain Kn via Eqs. (8) and (9), the correct evaluation of Kn is important and requires a proper value of the characteristic length d. However, unlike the ε/τ ratio, the characteristic length cannot be related solely to the porosity as indicated in Fig. 8(d).

Finally, the present study deals with gas diffusivities and porosity-to-tortuosity ratios for the dry and partially wet porous media with the same apparent porosities. Although the lattice DFT generally provides a qualitative description of capillary phenomena, we believe that the above-mentioned comparison is feasible as long as the void fractions are identical for the dry and partially wet structures, since the lattice gas model is able to represent how capillary condensation proceeds from smaller pores to larger ones, appropriately describing variations of void networks. For instance, Zeidman *et al.* investigated liquid adsorption in porous media using on-lattice coarse-grained Monte Carlo and found that calculated soil-water retention curves, which relate the soil suction to the volumetric liquid content, show good agreement with experimental counterparts [27].

IV. CONCLUSIONS

We have investigated the effect of capillary condensation on gas diffusivity in porous media composed of randomly packed spheres with moderate wettability. The lattice DFT simulations successfully reproduce the realistic adsorption/desorption isotherms and provide the fluid density distributions inside the porous media. We have found that capillary condensations lead to the occlusion of narrow pores because they preferentially occur at confined spaces surrounded by the solid walls. This tendency results in the larger values of the characteristic lengths d of the partially wet structures compared to those of the corresponding dry structures with the same porosities. Furthermore, the MSD simulations indicate that the effective diffusion coefficients are significantly suppressed by the partially condensed liquid; however, they are larger than those in the dry structures with the same porosities. Most importantly, we find that the ratio of the porosity to the tortuosity factor, ε/τ, which is a crucial parameter that determines the effective diffusion coefficient, can be reasonably related to the porosity even for the partially wet porous media. This finding is of great significance because it may enable the estimation of the value of ε/τ in the presence of capillary condensed liquid by referring to the corresponding value of a dry porous medium with the same material and porosity.

ACKNOWLEDGMENTS

This work was partly supported by the New Energy and Industrial Technology Development Organization (NEDO) of Japan and JSPS KAKENHI Grant No. 16K18009.

[1] J.-R. Li, R. J. Kuppler, and H.-C. Zhou, Chem. Soc. Rev. **38**, 1477 (2009).
[2] J. Lee, J. Kim, and T. Hyeon, Adv. Mater. **18**, 2073 (2006).
[3] R. Dittmeyer, V. Höllein, and K. Daub, J. Mol. Catal. A: Chem. **173**, 135 (2001).
[4] G. Q. Lu, J. C. Diniz da Costa, M. Duke, S. Giessler, R. Socolow, R. H. Williams, and T. Kreutz, J. Colloid Interface Sci. **314**, 589 (2007).
[5] T. Kotaka, Y. Tabuchi, and P. P. Mukherjee, J. Power Sources **280**, 231 (2015).
[6] A. Bertei, B. Nucci, and C. Nicolella, Chem. Eng. Sci. **101**, 175 (2013).
[7] Y. Gao, Int. J. Heat Mass Transfer **88**, 122 (2015).
[8] J. Valuš and P. Schneider, Appl. Catal. **1**, 355 (1981).
[9] K. Soukup, P. Schneider, and O. Šolcová, Chem. Eng. Sci. **63**, 1003 (2008).
[10] S. Komini Babu, H. T. Chung, P. Zelenay, and S. Litster, ACS Appl. Mater. Interfaces **8**, 32764 (2016).
[11] W. K. Epting, J. Gelb, and S. Litster, Adv. Funct. Mater. **22**, 555 (2012).
[12] T. Koido, T. Furusawa, and K. Moriyama, J. Power Sources **175**, 127 (2008).
[13] M. Sabharwal, L. M. Pant, A. Putz, D. Susac, J. Jankovic, and M. Secanell, Fuel Cells **16**, 734 (2016).
[14] S. Vierrath, F. Güder, A. Menzel, M. Hagner, R. Zengerle, M. Zacharias, and S. Thiele, J. Power Sources **285**, 413 (2015).
[15] H. Ostadi, P. Rama, Y. Liu, R. Chen, X. X. Zhang, and K. Jiang, J. Membr. Sci. **351**, 69 (2010).
[16] W. S. Jodrey and E. M. Tory, Simulation **32**, 1 (1979).

[17] J. M. Zalc, S. C. Reyes, and E. Iglesia, Chem. Eng. Sci. **59**, 2947 (2004).
[18] A. Berson, H.-W. Choi, and J. G. Pharoah, Phys. Rev. E **83**, 026310 (2011).
[19] M. M. Tomadakis and S. V. Sotirchos, AIChE J. **37**, 74 (1991).
[20] M. M. Tomadakis and T. J. Robertson, J. Compos. Mater. **39**, 163 (2005).
[21] H. Li, Y. Tang, Z. Wang, Z. Shi, S. Wu, D. Song, J. Zhang, K. Fatih, J. Zhang, H. Wang, Z. Liu, R. Abouatallah, and A. Mazza, J. Power Sources **178**, 103 (2008).
[22] W. Dai, H. Wang, X.-Z. Yuan, J. J. Martin, D. Yang, J. Qiao, and J. Ma, Int. J. Hydrogen Energy **34**, 9461 (2009).
[23] M. A. Hickner, N. P. Siegel, K. S. Chen, D. S. Hussey, D. L. Jacobson, and M. Arif, J. Electrochem. Soc. **155**, B427 (2008).
[24] I. Manke, C. Hartnig, M. Grünerbel, W. Lehnert, N. Kardjilov, A. Haibel, A. Hilger, J. Banhart, and H. Riesemeier, Appl. Phys. Lett. **90**, 174105 (2007).
[25] T. Sasabe, S. Tsushima, and S. Hirai, Int. J. Hydrogen Energy **35**, 11119 (2010).
[26] T. Hutzenlaub, J. Becker, R. Zengerle, and S. Thiele, J. Power Sources **227**, 260 (2013).
[27] B. D. Zeidman, N. Lu, and D. T. Wu, J. Chem. Phys. **144**, 174709 (2016).
[28] P. A. Monson, Microporous Mesoporous Mater. **160**, 47 (2012).
[29] R. J. R. Uhlhorn, K. Keizer, and A. J. Burggraaf, J. Membr. Sci. **66**, 259 (1992).
[30] P. Uchytil, R. Petrickovic, S. Thomas, and A. Seidel-Morgenstern, Sep. Purif. Technol. **33**, 273 (2003).
[31] P. Tarazona, Phys. Rev. A **31**, 2672 (1985).
[32] R. Evans, U. M. B. Marconi, and P. Tarazona, J. Chem. Phys. **84**, 2376 (1986).
[33] Y. Rosenfeld, Phys. Rev. Lett. **63**, 980 (1989).
[34] P. I. Ravikovitch and A. V. Neimark, Langmuir **22**, 11171 (2006).
[35] A. G. Salinger and L. J. Douglas Frink, J. Chem. Phys. **118**, 7457 (2003).
[36] L. J. Douglas Frink and A. G. Salinger, J. Chem. Phys. **118**, 7466 (2003).
[37] J.-P. Hansen and I. R. McDonald, *Theory of Simple Liquids*, 4th ed. (Academic Press, Amsterdam, 2013).
[38] K. Yamashita and H. Daiguji, J. Phys. Chem. C **117**, 2084 (2013).
[39] M. H. Factorovich, E. Gonzalez Solveyra, V. Molinero, and D. A. Scherlis, J. Phys. Chem. C **118**, 16290 (2014).
[40] Y. Zeng, L. Prasetyo, S. J. Tan, C. Fan, D. D. Do, and D. Nicholson, Chem. Eng. Sci. **158**, 462 (2017).
[41] P. A. Monson, J. Chem. Phys. **128**, 84701 (2008).
[42] U. M. B. Marconi and F. Van Swol, Phys. Rev. A **39**, 4109 (1989).
[43] E. Kierlik, P. A. Monson, M. L. Rosinberg, L. Sarkisov, and G. Tarjus, Phys. Rev. Lett. **87**, 055701 (2001).
[44] H.-J. Woo and P. A. Monson, Phys. Rev. E **67**, 041207 (2003).
[45] A. Einstein, *Investigations on the Theory of the Brownian Movement* (Dover, New York, 1926).
[46] M. M. Tomadakis and S. V. Sotirchos, AIChE J. **39**, 397 (1993).
[47] J. G. Powles, Chem. Phys. Lett. **125**, 113 (1986).
[48] W. G. Pollard and R. D. Present, Phys. Rev. **73**, 762 (1948).
[49] P. N. Henrion, Powder Technol. **16**, 159 (1977).
[50] B. Derjaguin, C. R. Acad. Sci. URSS **53**, 623 (1946).
[51] P. Levitz, J. Phys. Chem. **97**, 3813 (1993).
[52] P. Levitz, Adv. Colloid Interface Sci. **76–77**, 71 (1998).
[53] M. Knudsen, *The Kinetic Theory of Gases: Some Modern Aspects*, 3rd ed. (Wiley, New York, 1950).
[54] J. Greenwood, Vacuum **67**, 217 (2002).
[55] M. Thommes, K. Kaneko, A. V. Neimark, J. P. Olivier, F. Rodriguez-Reinoso, J. Rouquerol, and K. S. W. Sing, Pure Appl. Chem. **87**, 1051 (2015).
[56] J. R. Edison and P. A. Monson, J. Chem. Phys. **141**, 24706 (2014).
[57] B. Lu and S. Torquato, J. Chem. Phys. **98**, 6472 (1993).
[58] A. Pavlovitch, R. Jullien, and P. Meakin, Physica A **176**, 206 (1991).
[59] H. Naono, M. Hakuman, M. Shimoda, K. Nakai, and S. Kondo, J. Colloid Interface Sci. **182**, 230 (1996).
[60] J. U. Keller, F. Dreisbach, H. Rave, R. Staudt, and M. Tomalla, Adsorption **5**, 199 (1999).